


Design and Assembly of SPT-3G Cold Readout Hardware

J. S. Avva¹  · **P. A. R. Ade**² · **Z. Ahmed**^{3,4,5} · **A. J. Anderson**^{7,8} ·
J. E. Austermann⁹ · **R. Basu Thakur**⁸ · **D. Barron**⁶ · **A. N. Bender**^{8,10} ·
B. A. Benson^{7,8,11} · **J. E. Carlstrom**^{8,10,11,12,13} · **F. W. Carter**^{8,10} · **T. Cecil**¹⁰ ·
C. L. Chang^{8,10,11} · **J. F. Cliche**¹⁴ · **A. Cukierman**¹ · **E. V. Denison**⁹ ·
T. de Haan¹ · **J. Ding**¹⁵ · **M. A. Dobbs**^{14,16} · **D. Dutcher**^{8,13} · **T. Elleflot**³¹ ·
W. Everett¹⁷ · **A. Foster**¹⁸ · **R. N. Gannon**¹⁵ · **A. Gilbert**¹⁴ · **J. C. Groh**¹ ·
N. W. Halverson^{17,19} · **A. H. Harke-Hosemann**^{10,21} · **N. L. Harrington**¹ ·
M. Hasegawa²³ · **K. Hattori**²⁵ · **J. W. Henning**⁸ · **G. C. Hilton**⁹ ·
W. L. Holzapfel¹ · **Y. Hori**²³ · **N. Huang**¹ · **K. D. Irwin**^{3,4,5} · **O. B. Jeong**¹ ·
M. Jonas⁷ · **T. Khaire**¹⁵ · **A. M. Kofman**^{21,22} · **M. Korman**¹⁸ · **D. Kubik**⁷ ·
S. Kuhlmann¹⁰ · **C. L. Kuo**^{3,4,5} · **A. T. Lee**^{1,24} · **A. E. Lowitz**⁸ ·
S. S. Meyer^{8,11,12,13} · **J. Montgomery**¹⁴ · **A. Nadolski**²¹ · **T. Natoli**²⁶ ·
H. Nguyen⁷ · **H. Nishino**²³ · **G. I. Noble**¹⁴ · **V. Novosad**¹⁵ · **S. Padin**⁸ ·
Z. Pan^{8,13} · **J. Pearson**¹⁵ · **C. M. Posada**¹⁵ · **A. Rahlin**^{7,8} · **K. Rotermund**²⁰ ·
J. E. Ruhl¹⁸ · **L. J. Saunders**^{8,10} · **J. T. Sayre**¹⁷ · **I. Shirley**¹ ·
E. Shirokoff^{8,11} · **G. Smecher**²⁷ · **J. A. Sobrin**^{8,13} · **A. A. Stark**²⁸ ·
K. T. Story^{3,4} · **A. Suzuki**^{1,24} · **Q. Y. Tang**^{8,11} · **K. L. Thompson**^{3,4,5} ·
C. Tucker² · **L. R. Vale**⁹ · **K. Vanderlinde**^{26,29} · **J. D. Vieira**^{21,22} ·
G. Wang¹⁰ · **N. Whitehorn**^{1,30} · **V. Yefremenko**¹⁰ · **K. W. Yoon**^{3,4,5} ·
M. R. Young²⁹

✉ J. S. Avva
javva@berkeley.edu

- ¹ Department of Physics, University of California, Berkeley, CA 94720, USA
- ² School of Physics and Astronomy, Cardiff University, Cardiff CF24 3YB, UK
- ³ Kavli Institute for Particle Astrophysics and Cosmology, Stanford University, 452 Lomita Mall, Stanford, CA 94305, USA
- ⁴ Department of Physics, Stanford University, 382 Via Pueblo Mall, Stanford, CA 94305, USA
- ⁵ SLAC National Accelerator Laboratory, 2575 Sand Hill Rd., Menlo Park, CA 94025, USA
- ⁶ UC Berkeley Space Sciences Lab, 7 Gauss Way, Berkeley, CA 94720, USA
- ⁷ Fermi National Accelerator Laboratory, MS209, P.O. Box 500, Batavia, IL 60510-0500, USA
- ⁸ Kavli Institute for Cosmological Physics, University of Chicago, 5640 S. Ellis Ave., Chicago, IL 60637, USA
- ⁹ National Institute of Standards and Technology, 325 Broadway, Boulder, CO 80305, USA
- ¹⁰ High-Energy Physics Division, Argonne National Laboratory, 9700 S. Cass Ave., Argonne, IL 60439, USA

Abstract The third-generation upgrade to the receiver on the South Pole Telescope, SPT-3G, was installed at the South Pole during the 2016–2017 austral summer to measure the polarization of the cosmic microwave background. Increasing the number of detectors by a factor of 10 to $\sim 16,000$ required the multiplexing factor to increase to 68 and the bandwidth of the frequency-division readout electronics to span 1.6–5.2 MHz. This increase necessitates low-thermal conductance, low-inductance cryogenic wiring. Our cold readout system consists of planar thin-film aluminum inductive–capacitive resonators, wired in series with the detectors, summed together, and connected to 4K SQUIDs by 10- μm -thick niobium–titanium (NbTi) broadside-coupled striplines. Here, we present an overview of the cold readout electronics for SPT-3G, including assembly details and characterization of electrical and thermal properties of the system. We report, for the NbTi striplines, values of $R \leq 10^{-4}\Omega$,

-
- ¹¹ Department of Astronomy and Astrophysics, University of Chicago, 5640 S. Ellis Ave., Chicago, IL 60637, USA
 - ¹² Enrico Fermi Institute, University of Chicago, 5640 S. Ellis Ave., Chicago, IL 60637, USA
 - ¹³ Department of Physics, University of Chicago, 5640 S. Ellis Ave., Chicago, IL 60637, USA
 - ¹⁴ Department of Physics, McGill University, 3600 Rue University, Montreal, Quebec H3A 2T8, Canada
 - ¹⁵ Material Science Division, Argonne National Laboratory, 9700 S. Cass Ave., Argonne, IL 60439, USA
 - ¹⁶ CIFAR Program in Cosmology and Gravity, Canadian Institute for Advanced Research, Toronto, ON M5G 1Z8, Canada
 - ¹⁷ CASA, Department of Astrophysical and Planetary Sciences, University of Colorado, Boulder, CO 80309, USA
 - ¹⁸ Physics Department, Case Western Reserve University, Cleveland, OH 44106, USA
 - ¹⁹ Department of Physics, University of Colorado, Boulder, CO 80309, USA
 - ²⁰ Department of Physics and Atmospheric Science, 6310 Coburg Rd., PO BOX 15000, Halifax, NS B3H 4R2, Canada
 - ²¹ Astronomy Department, University of Illinois, 1002 W. Green St., Urbana, IL 61801, USA
 - ²² Department of Physics, University of Illinois, 1110 W. Green St., Urbana, IL 61801, USA
 - ²³ High Energy Accelerator Research Organization (KEK), Tsukuba, Ibaraki 305-0801, Japan
 - ²⁴ Physics Division, Lawrence Berkeley National Laboratory, Berkeley, CA 94720, USA
 - ²⁵ National Institute of Advanced Industrial Science and Technology, Tsukuba, Ibaraki 305-8563, Japan
 - ²⁶ Dunlap Institute for Astronomy and Astrophysics, University of Toronto, 50 St George St., Toronto, ON M5S 3H4, Canada
 - ²⁷ Three-Speed Logic, Inc., Vancouver, BC V6A 2J8, Canada
 - ²⁸ Harvard-Smithsonian Center for Astrophysics, 60 Garden St., Cambridge, MA 02138, USA
 - ²⁹ Department of Astronomy and Astrophysics, University of Toronto, 50 St George St., Toronto, ON M5S 3H4, Canada
 - ³⁰ Department of Physics and Astronomy, University of California, Los Angeles, CA 90095, USA
 - ³¹ Department of Physics, University of California, San Diego, CA 92093-0424, USA

$L = 21 \pm 1$ nH, and $C = 1.47 \pm .02$ nF. Additionally, the striplines’ thermal conductivity is described by $kA = 6.0 \pm 0.3 T^{0.92 \pm 0.04} \mu\text{W mm K}^{-1}$. Finally, we provide projections for cross talk induced by parasitic impedances from the stripline and find that the median value of percentage cross talk from leakage current is 0.22 and 0.09% from wiring impedance.

Keywords SPT-3G · Cosmic microwave background · Frequency-division multiplexing

1 Introduction

The South Pole Telescope is a 10-m telescope in Antarctica at the Amundsen-Scott South Pole Station. The third-generation receiver on the South Pole Telescope, SPT-3G, was commissioned during the 2016–2017 austral summer to study polarization of the cosmic microwave background [1]. As part of the upgrade, the number of detectors increased by a factor of 10 to $\sim 16,000$. This requires a larger multiplexing factor, necessitating the development of new cryogenic readout electronics.

The SPT-3G camera is composed of superconducting transition-edge sensors (TESs) thermally isolated on suspended SiN membranes operating under negative electrothermal feedback. For this number of detectors operating at cryogenic temperatures, multiplexing readout must be implemented. SPT-3G uses frequency-division multiplexing [2–5]. Each detector is part of a resonant LCR circuit, where the series capacitor and inductor dictate the resonant frequency for each bolometer. An AC current bias provided via direct digital synthesis (the “carrier” in the left panel of Fig. 1) is passed through a small bias resistor and the parallel combination of the detector comb, thereby providing a stiff voltage bias to each detector at the resonant frequency of its LCR circuit. Baseband feedback on each bolometer reduces the current through the SQUID by injecting a “nuller” signal to exactly cancel the carrier at the summing junction before the SQUID. After the SQUID, the residuals

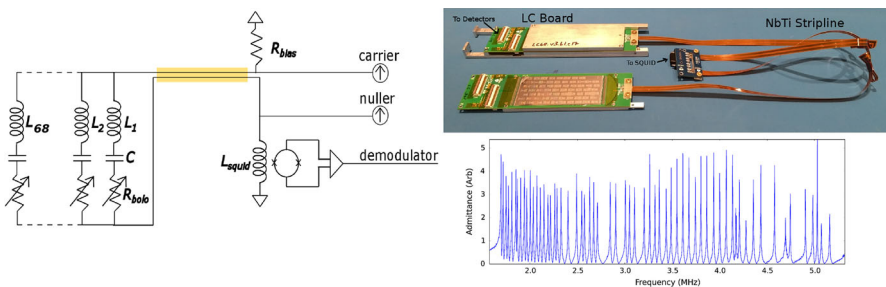


Fig. 1 Left: Basic schematic of the digital frequency-division multiplexing system. The stripline location is the shaded orange box. Right Top: Picture of the cold readout hardware, courtesy of Amy Bender [2]. Two LC boards on the left are connected to the PCB on the right that will connect to the SQUIDS. Right Bottom: Network analysis of one readout module. The resonant peaks of each individual bolometer’s LCR circuit form a “comb” of resonances (Color figure online)



Fig. 2 Left: Cross-sectional diagram of the layers of the NbTi stripline. Center: Top of the *LC* board PCB connected to the stripline with ultrasonic solder joints. Right: Bottom of the *LC* board PCB connected to the stripline with ultrasonic solder joints (Color figure online)

are demodulated at each carrier frequency. Sky signals modulate the TES resistance such that they appear as sidebands on the carrier tone. The “nuller” tone needed to cancel the modulated carrier tone at the SQUID is the science signal. Since the readout has a multiplexing factor of 68, when a network analysis is taken of one readout module, a “comb” of resonant peaks appear, as seen in the bottom right panel of Fig. 1.

The *LCR* circuit on the left panel of Fig. 1 maps to physical hardware pictured on the top right panel of Fig. 1. Each detector (not pictured) is depicted as a variable resistor. The inductances and capacitances are set the lithographed (*LC*) circuit (modules on the left side of the hardware photo in Fig. 1) [6]. The wiring between the 4K SQUIDs and the ~ 300 mK *LC* boards is a Niobium–Titanium (NbTi) broadside-coupled stripline (shaded box on the circuit diagram, right side of the hardware photo in Fig. 1). The stripline has nonzero inductance and capacitance as well, which manifests as a stray inductance and capacitance in the circuit.

2 Assembly of the SPT-3G Cold Readout Hardware

For the SPT-3G receiver, 120 *LC* modules are attached to 120 striplines. The striplines are made of NbTi.¹ NbTi is an attractive low-resistance wiring choice due to its superconducting temperature of 10K. However, attaching the NbTi stripline to the *LC* module, as seen in Fig. 2, is non-trivial because NbTi oxidizes. To combat this, connection methods utilizing ultrasonic solder are implemented. The method of ultrasonic soldering involves a solder formulated with metallic oxides and a specialized soldering iron.² The soldering iron vibrates at ultrasonic frequencies (tens of kHz), which causes cavitation in the molten solder. This disrupts the oxide on the metal and allows the ultrasonic solder to adhere to the NbTi surface. Once the stripline has been tinned with ultrasonic solder, conventional solder can be used to attach the striplines to the

¹ NbTi rolled by Rikazai Co., Ltd, and stripline manufactured by PrimeTech Corporation.

² We used the Cerasolzer USS-9210 Ultrasonic Soldering System and Cerasolzer CS297-150 solder.

Table 1 Measured parameters of NbTi striplines

Parameter	Value
Capacitance	1.47 ± 0.02 nF
Inductance	21 ± 1 nH
Resistance	$< 10^{-4}$ Ω
Thermal conductivity \times cross-sectional area	$kA = 6.0 \pm 0.3 T^{0.92 \pm 0.04}$ $\mu\text{W mm K}^{-1}$ for 0.5 to 5 K

pads on the PCB leading to the SQUID or LC board. Examples of this connection are pictured in Fig. 2.

3 Characterization and Performance of the SPT-3G Cold Readout Hardware

While multiplexed readout minimizes the thermal load from wiring, control of stray resistances, capacitances, and inductances is essential to minimize cross talk. Here, we present characterization of the NbTi striplines to show the value of inductance meets the targeted maximum parasitic series inductance of 60 nH [2], and that the stripline and solder joint resistance are zero within measurement error. Values for the capacitance, inductance, resistance, and thermal conductivity are given in Table 1.

3.1 Characterization of Niobium–Titanium Striplines

Broadside-coupled NbTi striplines connect the 4K SQUIDs to the ~ 300 mK LC boards. Each line is 60 cm long and 2 mm wide, with a 30 μm core between each differential pair, as seen in the cross-sectional diagram in Fig. 2. To minimize the wiring inductance, the wires are close together so that the magnetic fields from their currents maximally cancel.

Two resonant circuits are compared to measure the inductance of the NbTi stripline. The first circuit terminates the SQUID with a 33-nF capacitor. The second attaches the stripline to the SQUID and terminates the stripline with a 33-nF capacitor. The capacitance value was chosen to create a resonance within the readout bandwidth of the electronics, and because it is a much larger value than the stripline capacitance of 1.47 nF. Measuring the resonant peak location, ν_L , determines the inductance L for the circuit, as seen in Eq. (1).

$$\nu_L = \frac{1}{2\pi\sqrt{L \times 33 \text{ nF}}} \quad (1)$$

The difference in the resonant peak locations of the two circuits determines the stripline inductance, pictured in the right panel of Fig. 3. The stripline inductance is measured to be 21 ± 1 nH, and the total parasitic inductance due to the stripline, connectors, and wiring on the SQUID mounting PCB is measured to be 46 ± 1 nH.

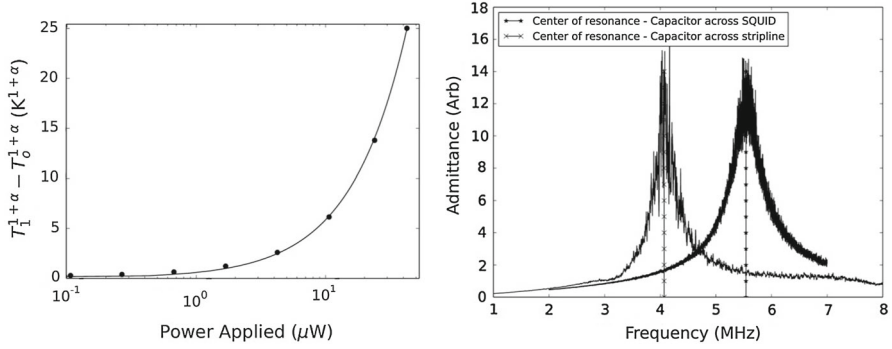


Fig. 3 Left: Data (points) and fit (line) relating the power deposited on the stripline to the difference between the temperature at the center of the stripline, T_1 , and the temperature at the edge, T_0 . Right: Two resonances formed by the LC circuit of the cold electronics including the stripline terminated with a 33-nF capacitor (left peak) and the cold electronics terminated with a 33-nF capacitor before the stripline at the SQUID (right peak). The inductance of only the stripline is measured by finding the shift of the resonant frequency due to the change in inductance

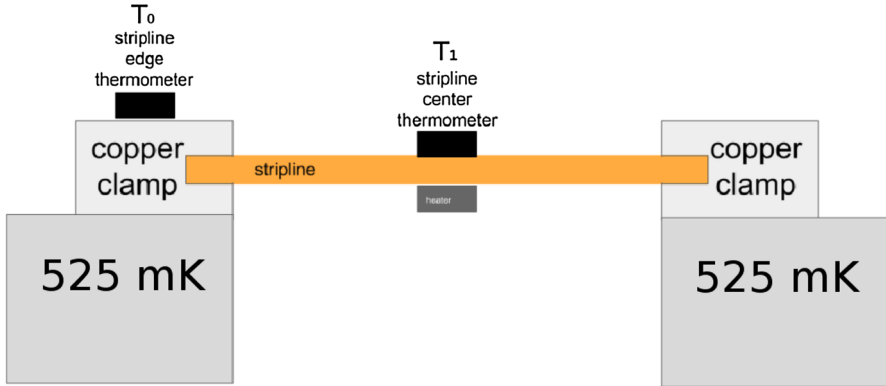


Fig. 4 Diagram of the stripline thermal conductivity measurement. A stack of 8 striplines is thermally sunk at each edge to 525 mK, and a heater is applied at the suspended center of the stack. Power is applied at the center, and the temperatures T_1 and T_0 are measured at the center and edge, respectively (Color figure online)

The thermal conductivity of the striplines impacts the millikelvin stage heat load. For cryogenic experiments, an important quantity to note is the product of the thermal conductivity k and the stripline cross-sectional area A , which describes the heat load for this specific application. This product is readily fit by a power law with normalization A_0 and exponent α .

$$kA = A_0 T^\alpha \quad (2)$$

To measure the stripline thermal conductivity, eight striplines are stacked, and both sides of the stack are thermally sunk to 525 mK. A heater and thermometer are attached at the suspended center of the stack, and an additional thermometer is attached at the edge of the stack. This experimental setup is shown in Fig. 4. The heater deposits power P onto the suspended center of the stripline. Temperature T_1 is measured at

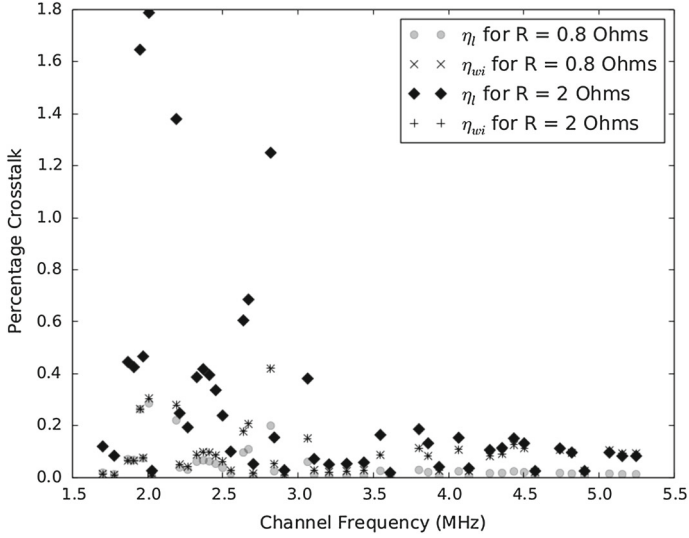


Fig. 5 Projected cross talk from measured parameters of a readout module in the SPT-3G receiver. Two resistances are plotted, to compare to previous simulations of design specifications (0.8 Ω), and representative SPT-3G bolometers (2 Ω). The outlier points that scatter above the design specification of 0.5% cross talk are due to fabrication scatter in frequency peaks and increased bolometer resistance

the center where the power is deposited, and temperature T_0 is measured at the edge. This is repeated for a variety of applied powers, and the relation between the power applied and the edge temperature measured can be fit to the integral of the power law described in Eq. (2), with the fit shown in Fig. 3. These data are best described by the fit $kA = 6.0 \pm 0.3 T^{0.92 \pm 0.04} \mu\text{W mm K}^{-1}$.

The total resistance of the stripline and solder joints is measured via a 4-point measurement with a Picowatt AVS-47 resistance bridge operating at 13.7 Hz. Liquid helium was used to cool the stripline below its critical temperature. This measurement results in an upper limit on the resistance of $< 0.0001 \Omega$.

3.2 Constraining Cold Readout Performance with Cross talk

For frequency-division multiplexed systems, careful control of stray inductances and capacitances are crucial to mitigate cross talk. Two forms of cross talk dominate frequency-division multiplexed readout systems—bias carrier leakage and nonzero wiring impedance. There is a third form of cross talk from the mutual inductance of inductors that are close in channel frequency and physically close on-chip. SPT-3G has diminished this mechanism by fabricating neighboring channels' inductors physically well separated on the chip [5,6]. The ratio of cross talk from bias carrier leakage, η_l , for a bolometer with resistance R_{bolo} , in series with inductor L , and with spacing in frequency to its nearest neighbor, $\Delta\Omega$, can be described by Eq. (3).

$$\eta_l = \frac{R_{\text{bolo}}^2}{2\Delta\Omega L} \quad (3)$$

The wiring impedance cross talk, η_{wi} , is described in terms of the current at frequency Ω_i on channel i , $I_{\text{Chi}}^{\Omega_i}$ with stray impedances L_{stray} by Eq. 4.

$$\eta_{\text{wi}} = -\frac{I_{\text{Chi}\pm 1}^{\Omega_i}}{I_{\text{Chi}}^{\Omega_i}} \frac{\Omega_i}{\Delta\Omega} \frac{L_{\text{stray}}}{L} \quad (4)$$

See Dobbs 2012 [4] for further discussion and derivation of these cross talk terms. For the SPT-3G system, a network analysis measures peak locations and frequency spacing for one module. As mentioned above, the stray inductance is 46 nH and each inductor in the LC board is 60 μH . The bolometers in the SPT-3G receiver are conservatively described by $R_{\text{bolo}} = 2 \Omega$. Cross talk calculated using a resistance of 0.8 Ω is additionally displayed to compare to the cross talk simulations in Bender 2016 [2]. Figure 5 shows the projected cross talk from both mechanisms as a function of frequency using these measured parameters. For $R_{\text{bolo}} = 2 \Omega$, the median value of percentage cross talk from leakage current is 0.22%, and from wiring impedance is 0.09%. Outlier channels that show cross talk above the design specification of 0.5% cross talk [2] are due to fabrication scatter in resonant frequency locations and increased bolometer resistance.

4 Conclusions

We present measurements of the cold wiring in the readout electronics for SPT-3G. The low measured values of inductance, resistance, and thermal conductivity of the NbTi striplines meet design specifications for the sensitive measurements that SPT-3G is designed to make. Careful control of parasitics is essential for the low levels of cross talk shown above.

Acknowledgements The South Pole Telescope is supported by the National Science Foundation (NSF) through Grant PLR-1248097. Partial support is also provided by the NSF Physics Frontier Center Grant PHY-1125897 to the Kavli Institute of Cosmological Physics at the University of Chicago, and the Kavli Foundation and the Gordon and Betty Moore Foundation Grant GBMF 947. Work at Argonne National Laboratory, including Laboratory Directed Research and Development support and use of the Center for Nanoscale Materials, a U.S. Department of Energy, Office of Science (DOE-OS) user facility, was supported under Contract No. DE-AC02-06CH11357. Work at Fermi National Accelerator Laboratory, a DOE-OS, HEP User Facility managed by the Fermi Research Alliance, LLC, was supported under Contract No. DE-AC02-07CH11359. NWH acknowledges support from NSF CAREER Grant AST-0956135. The McGill authors acknowledge funding from the Natural Sciences and Engineering Research Council of Canada, Canadian Institute for Advanced Research, and Canada Research Chairs program. We acknowledge R. Divan, L. Stan, C.S. Miller, and V. Kutepova for supporting our work in the Argonne Center for Nanoscale Materials. D. Barron is supported by an NSF Astronomy and Astrophysics Postdoctoral Fellowship under award AST-1501422. This material is based upon work supported by the National Science Foundation Graduate Research Fellowship under Grant Nos. DGE 1752814 and DGE 1106400. Useful conversations are acknowledged with Xiaoyu Guo.

References

1. B.A. Benson, P.A.R. Ade, Z. Ahmed, S.W. Allen, K. Arnold, J.E. Austermann, A.N. Bender, L.E. Bleem, J.E. Carlstrom, C.L. Chang, et al., Spt-3g: a next-generation cosmic microwave background polarization experiment on the south pole telescope, in *SPIE Astronomical Telescopes + Instrumentation, International Society for Optics and Photonics*, (2014), pp. 91531P–91531P
2. A.N. Bender, P.A.R. Ade, A.J. Anderson, J. Avva, Z. Ahmed, K. Arnold, J.E. Austermann, R. Basu Thakur, B.A. Benson, L.E. Bleem, et al., Integrated performance of a frequency domain multiplexing readout in the spt-3g receiver, in *International Society for Optics and Photonics Millimeter, Submillimeter, and Far-Infrared Detectors and Instrumentation for Astronomy VIII*, vol. 9914, (2016), p. 99141D
3. A.N. Bender, J.-F. Cliche, T. de Haan, M.A. Dobbs, A.J. Gilbert, J. Montgomery, N. Rowlands, G.M. Smecher, K. Smith, A. Wilson, Digital frequency domain multiplexing readout electronics for the next generation of millimeter telescopes, in *SPIE Astronomical Telescopes+ Instrumentation, International Society for Optics and Photonics*, (2014), pp. 91531A–91531A
4. M.A. Dobbs, M. Lueker, K.A. Aird, A.N. Bender, B.A. Benson, L.E. Bleem, J.E. Carlstrom, C.L. Chang, H.-M. Cho, J. Clarke et al., Frequency multiplexed superconducting quantum interference device readout of large bolometer arrays for cosmic microwave background measurements. *Rev. Sci. Instrum.* **83**(7), 073113 (2012)
5. K. Hattori, Polarbear collaboration, et al., Frequency domain multiplexed readout of kilopixel arrays of transition edge sensor bolometers, in *Society of Photo-Optical Instrumentation Engineers (SPIE) Conference Series, Society of Photo-Optical Instrumentation Engineers (SPIE) Conference Series*, (2014)
6. K. Rotermund, B. Barch, S. Chapman, K. Hattori, A. Lee, N. Palaio, I. Shirley, A. Suzuki, C. Tran, Planar lithographed superconducting lc resonators for frequency-domain multiplexed readout systems. *J. Low Temp. Phys.* **184**(1–2), 486–491 (2016)